Impacts of Thunderstorm-Generated Gravity Waves on the Ionosphere-Thermosphere using TIEGCM-NG/MAGIC Simulations and Comparisons with GNSS TEC, ICON and COSMIC-II Observations

Xian Lu[1], Haonan Wu[1,2], Chris Heale[3], Scott England[4], Shunrong Zhang[5]

1. Department of Physics and Astronomy, Clemson University, Clemson, SC, USA
2. High Altitude Observatory, NSF National Center for Atmospheric Research, Boulder, CO, USA
3. Center for Space and Atmospheric Research, Embry-Riddle Aeronautical University, Daytona Beach, FL, USA
4. Department of Aerospace and Ocean Engineering, Virginia Polytechnic Institute and State University, Blacksburg, VA, USA
5. MLT Haystack Observatory, USA

Abstract

We use the TIEGCM-NG nudged by MAGIC gravity waves to study the impacts of a severe thunderstorm system, with a hundred tornado touchdowns, on the ionospheric and thermospheric disturbances. The generated waves induce a distinct concentric ring pattern on GNSS TIDs with horizontal scales of 150–400 km and phase speeds of 150–300 m/s, which is well simulated by the model. The waves show substantial vertical evolution in period, initially dominated by 0.5 h at 200 km, shifting to 0.25 h at higher altitudes, and generating higher-frequency modes at 400 km. The TADs reach amplitudes of 100 m/s, 60 m/s, 80 K, and 10% in horizontal winds, vertical wind, temperature, and relative neutral density, respectively. Significantly perturbations in electron density cause dramatic changes in its nighttime structure

around 200 km and near the EIA crest. The concentric TIDs are also simulated in ion drifts and mapped from the Tornado region to the conjugate hemisphere likely due to neutral wind-induced electric field perturbations. The waves manage to impact the ionosphere at altitudes of ICON and COSMIC-II, which pass through the region of interest on a total of 8 separate orbits. In situ ion density observations from these spacecrafts reveal periodic fluctuations that frequently show good agreement with the TIEGCM-NG simulation. The O^+ fraction observations from ICON indicate that the density fluctuations are the result of vertical transport of the ions in this region, which could result from either direct forcing by neutral winds or electrodynamic coupling.

Plain Language

The ubiquitous gravity waves are often generated in the lower atmosphere of the Earth by activities associated with terrestrial weather and play an important role in transporting energy and momentum to the upper atmosphere. Transient fluctuations and coupling to plasma motions induced by gravity waves can cause significant disturbances to ionospheric scintillation, satellite orbits, and space infrastructure. In this work, we couple a neutral wave model to an ionosphere-thermosphere model through a nudging technique, to simulate the lifecycle of a gravity wave packet generated by a severe thunderstorm system over the US continent. The simulated wave characteristics match multi-layer observations including those in the stratosphere (AIRS), F-region (GNSS TEC), and topside of the ionosphere (COSMIC-II, ICON), indicating a profound effect of vertical wave coupling. The waves not only cause significant neutral and plasma fluctuations in the near-field, but also reach the conjugate hemisphere, where salient TID features are mirrored likely via the neutral wind-induced electric field perturbations. This work shows that the global impact of regional terrestrial weather via plasma-neutral coupling and geomagnetic field-line mapping mechanisms. Leveraging the nudging capability of the ionosphere-thermosphere model, our approach provides a robust framework to incorporate lower-atmosphere waves realistically and explore their far-reaching impacts.

1. Introduction

Gravity waves (GWs) are ubiquitous in the Earth's atmosphere and play an important role in modulating the middle-atmosphere circulation and transporting momentum and energy (Fritts and Alexander, 2003). One of the important wave sources is embedded in terrestrial weather such as tornadoes, thunderstorms, and hurricanes, and the waves generated are often characterized by concentric or semi-concentric ring patterns (Vadas et al., 2012; Yue et al., 2014; Gong et al., 2015; Azeem et al., 2015). GWs propagate upward with increasing amplitudes due to the decrease of atmospheric density. This increase typically counteracts wave dissipation allowing GWs to reach significant magnitudes in the ionosphere and thermosphere region (Lu et al., 2009, 2015b; Chen et al., 2013; 2016). The neutral perturbations couple to traveling ionospheric disturbances (TIDs) with typical horizontal wavelengths of 100–400 km, phase speeds of 100–500 m/s, and amplitudes of 0.1–3.5 TECu in Total Electron Content (TEC) (Azeem et al., 2015; Chou et al., 2017; Heale et al. 2019). These perturbations also give rise to large vertical plasma drifts, seeding of equatorial plasma bubbles, and increased radio scintillation (Nicholls and Kelley, 2005; Bishop et al., 2006; Takahashi et al., 2020; Huba et al., 2023a). Satellite observations such as the Atmospheric Infrared Sounder (AIRS), Cloud Imaging and Particle Size (CIPS) instrument, Global Ultraviolet Imager (GUVI), Global-scale Observations of the Limb and Disk (GOLD), as well as ground-based airglow imagers, are invoked to observe the neHutral counterparts of GWs known as Traveling Atmospheric Disturbances (TADs) (Yue et al., 2014; England et al., 2021; Bossert et al., 2022;

Cullens et al., 2023). Coherency of wave structure, timing, and location are often identified in the concurrent Global Navigation Satellite System (GNSS) TEC measurements, suggesting the link between them and the same origins (Azeem et al., 2015; England et al., 2021; Harvey et al., 2023).

Numerical modeling has been used to simulate GWs excited by convective sources and examine the wave impacts in a more systematic way. Heale et al. (2019) studied GWs generated by a thunderstorm system over the midwestern United States using Model for Acoustic-Gravity wave Interactions and Coupling (MAGIC) (Snively & Pasko, 2008; Snively, 2013; Heale & Snively, 2015) and the model results compared favorably with the multi-layer observations. Liu et al. (2014) used the high-resolution Whole Atmosphere Community Climate Model (WACCM) and simulated the GW generation by a tropical cyclone, which reached a planetary-scale extent in the mesosphere and lower thermosphere. Liu et al. (2024) investigated resolved GWs (down to ~200 km in horizontal wavelength) on circulation and composition using the high-resolution WACCM with thermosphere/ionosphere extension (WACCM-X) and demonstrated significant vertical evolution of the phase speed spectra. A similar range of GW spectra are also simulated by the HIgh Altitude Mechanistic general Circulation Model (HIAMCM) in which medium-scale GWs are shown to compare well with the AIRS observations (Becker et al., 2022).

Recent efforts have been devoted to coupling neutrals to ionosphere and thermosphere or plasmasphere models for a detailed examination of the ionospheric consequential phenomena such as plasma bubbles and TIDs with origins from below. Zhao et al. (2020) added a specified GW matching the GPS-TEC measurements to the lower boundary of Global Ionosphere-Thermosphere Model with local-grid refinement (GITM-R) and reproduced the tropical cyclone-induced concentric GWs and TIDs. Wu et al. (2023) nudged high-resolution WACCM-X neutral winds and temperatures to the Thermosphere-Ionosphere-Electrodynamics General Circulation Model with a nested-grid extension (TIEGCM-NG) for the Hunga Tonga-Hunga Ha'apai (Tonga) volcano eruption event. The model results capture large perturbations in vertical neutral winds (~100 m/s) and TIDs reaching over 10 TECu in amplitudes consistent with the GNSS observations. Huba et al. (2023b) modeled the development of an equatorial plasma bubble during a midnight temperature maximum via the coupled SAMI3/WACCM-X model. Vadas et al. (2023) and Huba et al. (2023a) used the coupled SAMI3/HIAMCM/MESORAC (Model for gravity wavE SOurce, Ray trAcing and reConstruction) model set and showed the effects of secondary GWs on the ionospheric perturbations and instability.

Previous studies have shown the impressive ionospheric responses to waves originating from the lower atmosphere. However, more case studies are still needed to enhance our understanding and develop a comprehensive perspective on the relationship between wave sources and their ionospheric impacts. Prominent science questions that remain to be addressed include understanding why similar terrestrial weather events can trigger diverse TID structures and magnitudes, how neutral background and ionospheric conditions affect wave propagation and neutral-ion coupling, and how wave characteristics and impacts evolve with altitudes. In this work, we couple the MAGIC (GW part in neutrals) to the TIEGCM-NG in a similar way as in Wu et al. (2023) except the GWs are obtained from a high-resolution regional model, instead of a global circulation model. We first compare the modeled TIDs with GNSS observations, using the model results to systematically investigate the wave impacts on neutral winds, temperature, density, electron density, and ion drifts. Additionally, we track the vertical evolution of the waves and identify their imprints on ICON and COSMIC-II measurements near the topside of the ionosphere.

2. Tornado Event, Data, and Model Runs

During 12/13 April 2020, a severe storm system in the Southeastern United States led to a deadly 'Easter Tornado Outbreak': throughout the two-day outbreak, a total of 141 tornadoes touched down across 10 states, inflicting widespread and locally catastrophic damage. The outbreak ranks 4th for producing the most tornadoes in a 24-hour period, with 132 tornadoes occurring between 14:40 UTC April 12–13 (Figure 1a). Figure 1b shows the reflectivity observations from the Next-Generation Radar (NEXRAD) network at 21:55 UTC on 12 April 2020, indicating the presence of a severe storm system over the southeastern United States that propagates in a southeastern direction as time progresses. During a similar time period, the AIRS observations show the concentric ring patterns in the stratosphere (~35 km altitude) at 18:00 UTC (Figure 1c).

2.1. GNSS dTEC Observations

World-wide ground-based GNSS TEC data have been produced at MIT Haystack Observatory using the MAPGPS software suite (Rideout et al., 2006; Vierinen et al., 2016), The GNSS TEC processing utilizes 6000+ global receivers, 3000+ in the American sector, using both the GPS and GLONASS constellations. TIDs are identified based on ionospheric disturbance information as represented by differential TEC (dTEC) values, with background TEC variations being detrended (Zhang et al., 2017). For this purpose, the background TEC is determined by using a low-pass filter (Savitzky and Golay, 1964) with a linear basis function within a 30-minute sliding window (Zhang et al., 2022; 2023). In order to be consistent with observations, once we obtain the TEC from the model run, we apply the similar methodology here to retrieve the dTECs using the model results.

The GNSS observations reveal the emergence of concentric TIDs around 22:00 UTC on 12 April, intensifying and reaching their peak by 01:00 UTC on 13 April, before gradually weakening thereafter (Figures 3a1-a3 and movie S1). The presence of concentric ring patterns in both the stratosphere and ionosphere, coinciding with the lower-atmosphere thunderstorm and tornado outbreak, implies that the generation of GWs and TIDs stems from the convective source.

2.2. ICON and COSMIC-II Observations

The Ionospheric Connection Explorer (ICON) Ion Velocity Meter (IVM) instrument is described by Heelis et al. (2017), with its performance by Heelis et al. (2022). The IVM measures the ion density, velocity, temperature, and fraction of the ions that are O^+ or H^+ at the spacecraft's location with a 1 second cadence. ICON is in a near-circular orbit at 27° inclination orbit, with an altitude between ~580 – 610 km. This study uses the Level 2, version 6 of the IVM data (the latest available at the time of writing). Only values of the ion density and O^+ fraction data that are reported as good quality are used.

The COSMIC-2 FM4 constellation of satellites (referred to as COSMIC-II hereafter) each carry similar IVM instruments to ICON, with its performance described by Chou et al. (2021). This study uses the Level 2m COSMIC-II data (the latest available at the time of writing). The COSMIC-II satellites have a near circular orbit at 24° inclination orbit, with an orbital altitude between ~520–550 km.

2.3. MAGIC Simulation

The MAGIC model simulates the nonlinear, compressible Navier-Stokes equations using a finite-volume approach through the clawpack routines (Leveque 2002) and applying the "f-wave method' of Bale et al. (2002). GWs within MAGIC are generated from NEXRAD precipitation rates at each grid location which are converted to a latent heating profile using the Stephan and Alexander (2015) algorithm. The latent heating profiles are then applied time-dependently to the Navier-stokes energy equation to drive GWs. We note that this approximation assumes that all GWs are driven by latent heating occurring due to precipitation within the storms. The simulation for this event runs from 20:00 UTC on 12 April to 01:30 UTC on 13 April and includes a 45-minute ramp up period to avoid unphysical acoustic waves being generated. The ambient atmospheric state is determined as a mean over Alabama during this time period and is defined as a combination of MERRA-2, HWM and MSIS winds, temperatures and densities. The simulation domain covers most of the continental United States (CONUS) with a 4km horizontal resolution and a 1km vertical resolution from the ground to 300 km altitude.

Figure 2 shows the MAGIC temperature at z=50 km, 100km, and 250 km at 21:55 UTC on 12 April 2020 with the NEXRAD reflectivity overlaid. The plots show semi-concentric wave patterns with preferential eastward propagation that originate from the storms below. A wavelet analysis at z=250 km altitude suggests dominant horizontal wavelengths between 150–400 km and amplitudes of ~80 K. At z =100 km, nonlinearity, instabilities, and wave breaking are present in the wave field which can generate secondary waves. Therefore, the waves seen at z=250 km are likely a mixture of primary waves propagating directly from the source and secondary waves generated from primary wave breaking and/or momentum/energy deposition in the Mesosphere and Lower Thermosphere. Secondary waves can be generated with a spectra of scales and periods depending on the dominant mechanism that generated them. Typically, primary wave saturation and dissipation can impart momentum and energy into the mean flow locally leading to re-radiation of the energy as larger waves. In addition, strong nonlinearity and wave breaking of the primary wave can lead to the transfer of energy to other wave modes typically of smaller scales. Secondary waves generated by both of these mechanisms have the ability to carry further momentum and energy upward into the thermosphere/ionosphere.

2.4. TIEGCM-NG Nudged by MAGIC Gravity Wave Perturbations

TIEGCM is a global 3D numerical model that simulates the coupled thermosphere/ionosphere system from ~97 to ~600 km altitude. It self-consistently solves the fully coupled nonlinear, hydrodynamic, thermodynamic and continuity equations of the neutral gas, the ion and electron energy equations, the O^+ continuity equation and ion chemistry, and the neutral wind dynamo (Richmond et al., 1992; Qian et al., 2014). Realistic F10.7 are used in all simulations. Incorporating data assimilated aurora and electric fields (Wu and Lu, 2022; Wu et al., 2022) is now available as an option for high-latitude drivers, providing an optimal setup during geomagnetic storms (Lu et al., 2023). For simplicity, we use the Heelis model for high-latitude electrical potential here due to the very quiet geomagnetic condition (Kp<2). The output frequency of the diagnostic terms is one minute.

TIEGCM with the nested grid module (TIEGCM-NG) has been developed and introduced in Wu et al. (2023). For this event, we run a horizontal resolution of 1.25° for the global grid and implement two levels of sub-grid meshes with horizontal resolutions of 0.6° and 0.3°, respectively. The time step of the global grid is 10s and inner levels quadruple the sub-cycles (2.5s, 0.625s) compared to the outer level. Vertical resolution of TIEGCM-NG is 1/8 scale height for all levels. MAGIC has a higher resolution than the TIEGCM-NG which resolves much smaller scales (tens of km). Since such small-scale phenomena are not dominant from the TEC observations (Section 3.1), and in order to avoid numerical instability induced by high-frequency fluctuations, we apply a 2D horizontal Gaussian smoothing filter with standard deviation of 8 km on the MAGIC perturbations before nudging them to the lower levels of TIEGCM-NG. Four scale heights of MAGIC data (~95–130 km) are used for the nudging and a vertical weighting function with an exponential decaying rate of 0.4 scale height ${}^{-(z-z_0)/0.4}$ is used. z is the log-pressure coordinate used in the model (-7< z <-3) and z_0=-7 is the lower boundary of the model.

Since the MAGIC simulation is performed in the northern American sector instead of globalwise, an additional horizontal weighting function is further implemented to minimize the boundary effect. The horizontal weighting function is applied within 15° of the MAGIC domain and takes a Gaussian form with a width of 5° and shape of $exp^{-(\triangle x/5)^2}$ in which $\triangle x$ is the shortest great-circle distance to the edges of the MAGIC domain in degree. The total weighting function applied to MAGIC fields is the product of vertical and horizontal weighting functions.

The TIEGCM-NG is also run with no GWs being nudged at the lower levels as a control case. The difference fields between the control run and the GW-nudged run then represent the wave-induced perturbations.

3. Model Results

3.1. TID Simulations and Comparison with GNSS

We show the results in the finest grid (level-2 nested grid) for the TIEGCM simulations except for ion drifts, where the global grid is used (Figure 11). Figure 3 shows the GNSS dTEC compared with the TIEGCM-NG simulations at three different times corresponding to the initial, evolving, and peak phases of the event, delineated by the escalating magnitudes of TIDs. It can be seen that the TIEGCM-NG reasonably simulates the concentric ring pattern, including the timing of its development and the horizontal wave structure. The observations show a maximum TID amplitude in dTEC of ~0.1 TECu, while the simulation slightly surpasses this reaching ~0.15 TECu. We select three trajectories from the GNSS and model simulated TIDs (shown as the black dashed lines in Figures 3a3 and 3b3) to examine the spectrum of horizontal scale. The longitude and latitude of each trajectory are used to calculate the real distance in kilometers prior to wavelet estimation. Figure 4 shows the wavelet spectra in terms of wave amplitudes. Due to variations in trajectories, the horizontal wavelengths can be slightly different. The dominant wave spectrum typically ranges between 150–400 km, aligning with the findings from stand-alone MAGIC simulations regarding temperature perturbations at 250 km (Section 2.3). In addition to this range, a large scale with a horizontal wavelength of 600–800 km is also discernible, albeit with weaker magnitudes. A movie showing the propagation of TIDs is included in the Supporting Information (SI).

Figure 5 shows the dTEC keograms progressing with latitudes at longitudes of -95°, -88° and -81° from the GNSS observations and model simulations during the same time window. The general tilting of the phase fronts is consistent between them, indicating a northward wave propagation above ~35° latitude. Southward propagation is seen below ~35° from simulation, which is consistent with Figure 3 (right column) about the center of the concentric ring. Despite significant gaps in observations below 30°, southward propagation can still be traced, as shown by the downward phases from 20 to 21 UTC southward of 30° in Figure 5a. From Figures 3a3 and 3b3, the vertical slices at a longitude of 88° (black dashed lines 1 and 2) are nearly perpendicular to the wave fronts, so we can use the keogram along this line to estimate the horizontal phase speeds (middle column of Figure 5), which range from ~150–300 m/s. The model si mulations and observations show good agreement about the phase speeds.

The stronger TIDs (absolute amplitudes) southward of 30° latitude are due to the amplified mean TEC background as it approaches the Equatorial Ionization Anomaly (EIA). Relative dTEC perturbations which remove such an asymmetry are derived by dividing the mean background calculated as the longitudinal averaged TEC and shown in the last row of Figure 5. Relative dTEC perturbations reach a maximum amplitude of ~4–5% from model results.

3.2. Regional to Global Neutral and Ionospheric Responses

Now the model has been shown to largely reproduce the TIDs as observed, we can use it to systematically diagnose the wave impacts and their vertical evolution. Figure 6 illustrates the wave-induced perturbations (TADs) in neutral zonal wind (UN), meridional wind (VN), vertical wind (WN), and temperature (TN) at 200 and 400 km in top and bottom rows, respectively. Similar concentric ring patterns are present, and larger-scale TADs tend to appear strongly at far-fields of the domain compared with the smaller ones at the center. These larger-scale waves are the ones emerging in the observational domains of the ICON and COSMIC-II measurements (Section 4). In general, the wave amplitudes reach ~100 m/s for UN and VN, ~60 m/s for WN, and ~80 K for TN. As altitude increases, small to medium-scale waves tend to weaken in horizontal winds and temperatures (1^{st}, 2^{nd} and 4^{th} columns), while become stronger in vertical winds (3^{rd} column). The movie showing the TAD evolution is included in the SI.

Figure 7 shows the vertical structures of the waves at a location of 85° longitude, 40° latitude. The strongest horizontal wind and temperature perturbations are found below 300 km, while obvious attenuations are found above it. Figures 7e and 7f show the neutral perturbations at 200 and 400 km, respectively. High-frequency waves appear and become strong in vertical winds, which can be also seen clearly in Figure 7c. The vertical evolution of the wave spectra is consistent with the GW's polarization relation, wherein the amplitude ratio of temperature to vertical wind is nearly inversely proportional to the intrinsic frequency, therefore the higher-frequency waves exhibit stronger perturbations in the vertical wind component (Vadas and Fritts 2005; Vadas, 2013; Lu et al., 2015a, 2017). From the wavelet analyses (Figure 8), the dominant wave periods are about 0.5 h, with weaker yet visible ones around 0.25 h at 200 km. At 400 km, the 0.25-h waves strengthen, and even higher-frequency modes appear, which may be generated internally from nonlinear processes since they are barely seen at 200 km.

Figure 9 shows the wave-induced perturbations in the absolute electron density. Significant responses are seen at 200 and 250 km at later stages, especially in the night-time sector at 200 km (Figure 9c1) and inside of the EIA crest at 250 km (Figure 9c2). The waves become less efficient in perturbing the overall structure of electron density at 400 km. The significant perturbations in relative neutral densities are also observed (Figure 10). The initial and evolving phases show a preferential propagation towards the east, with waves appearing stronger on the eastern side of the domain. At the peak phase, the wave magnitude reaches an order of ~10% in some regions at 250 km and this magnitude of perturbations becomes more typical at 400 km (Figure 10, 3rd column), which has the potential to induce non-trivial orbital deviations for satellites due to the drag effect. To give a reference, Leonard et al. (2012) studied the operational consequences of longitude-dependent tides through a series of orbital and reentry predictions. They found that the in-track prediction differences by tidal effects are of order 200±100 m for satellites in 400-km orbits and 15±10 km for satellites in 200-km orbits for a 24-hour prediction. The maximum tidal amplitudes in relative neutral densities in their case reach 10-15% in the mesosphere and lower thermosphere region and become about half in the region of 300–400 km. The detailed analysis of the impacts from this tornado event featured by small-scale GWs is beyond the scope but deserves a further investigation.

To further analyze the wave impacts on the ionosphere, we show the perturbations in ion drifts in the zonal, meridional, and vertical directions (UI, VI, and WI) in Figure 11. The geographic coordinate in the global grid is used for the TIEGCM outputs. The near-field perturbations show concentric ring patterns while the planetary-scale perturbations are visible at lower latitudes, especially at later stages (a movie showing the time evolution is included in the SI). The conjugate hemispheric disturbances in ion drifts are likely caused by the electric fields originating in the Northern-Hemisphere tornado region. Neutral wind perturbations in GWs over this region can excite electric fields on the nightside which are mapped to the conjugate hemisphere through the Earth's magnetic field lines, producing plasma density fluctuations (i.e., MSTIDs). The GW induced electric fields were reported previously in both observations and simulations (e.g., Varney et al., 2009; Huba et al., 2015; Zhang et al., 2021). The similar conjugate effect and the resultant interhemispheric coupling are also simulated by the high-resolution WACCM-X for the Hunga Tonga-Hunga Ha'apai volcano eruption event (Liu et al., 2023). Liu et al. (2023) attributed the underestimation of the magnitude of the total E × B drift perturbations to the model's inability to capture small scales as observed (Shinbori et al., 2022). A similar issue exists, and the underestimation is also expected in our case.

It should be noted that the nested module hasn't implemented the neutral wind dynamo yet, thus the neutral perturbations must propagate to the global grid and then influence plasma motions, during which the perturbations are largely smoothed when mapped to a coarser grid. The use of a global grid with a resolution of 1.25° in this study would lead to a significant underestimation compared to the finer grid (0.3°), which is nearly one order of magnitude smaller. This suggests that much more significant perturbations in ion drifts (on the order of 100 m/s) and smaller-scale TIDs are anticipated responding to this event. It remains to be uncovered in the future how significant small-scale GWs can impact the neutral wind dynamo, and further model development is underway.

4. Wave Imprints in ICON and COSMIC-II Observations

While ground-based TEC observations are well suited to reveal the 2D horizontal structure of TIDs and their motion, these data represent an integral of the wave's impact across the entire ionosphere. By contrast, in situ ion measurements provide the wave characteristics at a single altitude (e.g., topside ionosphere), but not usually the 2D horizontal structure or motion of TIDs, and thus are a good complement to the TEC observations. Both ICON and COSMIC-II IVM data have been shown to be suitable for identifying TIDs in the topside ionosphere (e.g., Feggeler and England, 2024). The in-situ ion observations from ICON and COSMIC-II can be compared to the TIEGCM-NG simulations of the TIDs produced during this event. It is worth noting here that the uppermost level of the model is around the altitude of COSMIC-II, but never reaches the altitude of ICON. For that reason, the comparison will focus on the perturbations to the ions, rather than the absolute magnitudes of the densities.

ICON passes through the region of the simulation on 3 successive orbits, with the relevant segment of each of those shown in Figure 12a. Each of these orbit segments includes the day/night terminator as well as changes in latitude. Thus, there are significant changes in the value of the ion density along each track that are not the focus of this analysis. To isolate the TID-induced perturbations from this large-scale variation, the ion measurements are detrended by producing a low-pass dataset using a 15 degree along-track boxcar smooth (which is large compared to most of the perturbations seen in the TIEGCM-NG) and subtracting this from the original 1-second data. The detrended data is shown in Figure 12b–d for the ion density and Figure 12h–j for the O^+ fraction. As ICON is near the O^+ to H^+ transition altitude, the fraction of the ionosphere that is O^+ is a good proxy for vertical transport of the ions. Comparing the corresponding plots for the ion density and O^+ fraction, it is clear that many of the small to medium scale fluctuations in the total density correspond to changes in the O^+ fraction, and thus are likely the result of vertical transport of ions, either from advection by the winds or electrodynamic coupling. As each of the paths of the spacecraft through the region of interest are necessarily curved tracks, it is not possible to directly identify horizontal wavelengths from these plots, and so the horizontal scale sizes of features as seen along these curved tracks are examined. Comparing the orbit tracks in Figure 12 to the electron density perturbations shown in Figure 9, it can be seen that the orbit tracks are quasi parallel to the density enhancements, thus we expect the along-track spatial scales seen by both ICON and TIEGCM-NG when sampled along the ICON track to be significantly larger than wavelength of the TID.

A comparison to the TIEGCM-NG model densities can help to identify if the spatial scales of the fluctuations seen by ICON are in general agreement with those in the model. To do this, the model data at the closest point in time are interpolated to the ICON latitude and longitude using a simple bilinear interpolation. All model data are taken from the uppermost level of the model, which is still ~100 km below the altitude of ICON, but provides the closest point for comparison, with the two datasets shown in Figure 12. To avoid windowing effects, wherever ICON is outside the TIEGCM-NG domain, the global model is sampled. The data are then detrended in the same manner as the observations. Following this, both detrended datasets are trimmed to include only the region inside the nested grid. As the spacecraft do not fly along a cardinal direction, the data in either longitude or latitude are not evenly spaced, so a Lomb-Scargle periodogram is used to identify the dominant spatial scales. These are shown in Figure 12e–g.

The same process described above is then repeated with each of the COSMIC-II spacecraft. For these, a total of 5 passes are found to intersect the region of interest, 3 from spacecraft 1, 2 from spacecraft 4. Figure 13 shows these passes, the corresponding detrended densities and periodograms comparing these to the TIEGCM-NG. As COSMIC-II is much lower, the O^+ fraction is of less utility and is not included. The ICON and COSMIC-II passes are in regions southward of the center of the tornado event, which fall within the far-fields of the wave domains. Therefore, relatively larger scales of waves, on the order of a thousand kilometers (~ 5–10 degrees) instead of the 150–400 km range observed around the center, are expected to show favorable comparisons between the model and observations.

In comparing the in situ data to the model, it is worth remembering that the COSMIC-II spacecraft are just slightly above the model top boundary (~20-50 km) whereas ICON is higher still (~80-110 km above the model boundary). Given that, we may expect generally better agreement between the model and COSMIC-II, compared to ICON, which is the case. Examining the detrended ion density (Figure 13 panels b-f), the approximate magnitude of the fluctuations seen in the data and model are overall similar. The model displays a higher fluctuation on some orbits (e.g. panel d) and the data on others (e.g. panel e), but over the five they are comparable. Given the difference in altitudes and perhaps minor differences in the exact timing of wave generation and propagation, it is perhaps not surprising that the phase of the features don't show good alignment (while individual features certainly do, many do not). Instead we examine the spatial scales of the fluctuations, as seen along the curved orbit tracks (referred to as along-track wavelength), to determine the similarity between the fluctuations seen by the spacecraft and those simulated in the model. The first orbit shows no apparent agreement between the model and data, the reason for which is not known. The second orbit shows more similarity, both in the detrended densities (panel c) and spectra (panel h). Both model and data see a feature with a scale of around 7.5 degrees, and the model sees a feature with a scale of around 10.5 degrees, which is bracketed by features in the model at around 9 and 11.5 degrees. The amplitudes of these features are also relatively similar. Both model and data see a feature with a scale of around 14.5 degrees, which is close to the 15 degree window used for detrending the data. In the third orbit, the model and data both see a feature around 7 - 8 degrees, although this is of higher amplitude in the model than the data. The model sees a second feature near 11.5 degrees which may be related to that seen in the data at 13 degrees. In the fourth orbit, the detrended ion densities show a high degree of visual similarity (panel e), with clear fluctuations of around 10 degrees in scale. The spectrum in panel j shows this clearly for the data, whereas the model has a peak near 13 degrees, that is of a similar magnitude. In the fifth orbit, the fluctuations in the detrended ion densities again show some visual similarity in terms of amplitude of fluctuation (panel f), but those seen in the data are more broadly spaced than those in the model, as is reflected in the spectrum (panel k). Again, the magnitude of the fluctuations in panel k is similar between the model and data. Examining the ICON orbits, the first orbit does not show clear similarity in the detrended ion densities or the spectrum (Figure 12 panels b, e), which may be the result of the orbit being relatively close to the edge of the high resolution domain (Figure 12 panel a). The second and third orbits pass through much more of the high resolution domain, and of these the second orbit shows reasonable agreement between the model and data. The detrended ion densities have some visible similarity (panel c), and the spectra with the two strongest peaks around 9 and 12-13 degrees. The amplitude of the spectra are different with the observations showing a much stronger peak at the longer wavelength, which could be related to the altitude difference and changing ionospheric conditions over this region. The third orbit from ICON starts 6 minutes after the model simulation ends, and continues until 34 minutes after its end, with all data compared to the final time step of the model. While the range of the fluctuation in the data and model (panel d) are similar, there is not good agreement in their spatial scales (panel g). Taken as a whole, we see a reasonable degree of similarity between the model and in situ observations, with the exception of cases near the edge of the simulated domain (in time and space), and the first orbit of COSMIC-II. This suggests that the model is capturing much of the TAD/TID spectrum that is present and which reaches the topside ionosphere.

5. Conclusions

We nudge the GWs generated by the MAGIC model to TIEGCM-NG and symmetrically evaluate the impacts of a severe thunderstorm-focused event on the IT system. We first compare the model results with the GNSS TEC observations and find reasonable agreement in the structure and evolution of TIDs, characterized by horizontal wavelengths of 150–400 km and phase speeds of 150–300 m/s. The dominant wave periods are around 0.5h and 0.25h at 200 km altitude, with higher-frequency waves more prominent at higher altitudes. The maximum wave amplitudes in neutral horizontal winds (UN and VN), vertical wind (WN), and neutral temperature (TN) are about 100 m/s, 60 m/s, and 80 K, respectively. Significant perturbations in the absolute electron density are seen at night-time and near the EIA crest close to the F-region peak. Wave-induced neutral density perturbations peak ~10% at 250 km, and such magnitude becomes typical at 400 km, which can potentially cause significant deviations in satellite orbits. The conjugate effect is simulated and TIDs are reproduced in both hemispheres, whereas their magnitude is underestimated in the current model run due to limited resolution.

This is the first-time that the GW signatures originating from a convective source below have been identified in the ICON and COSMIC-II observations. Both ICON and COSMIC-II provide ion measurements in the topside ionosphere. These show periodic signatures along their respective orbit tracks that show a good degree of agreement with the TIEGCM-NG model. The ICON density and O^+ fraction fluctuations show a high degree of similarity, which is indicative of the density changes originating from vertical transport of the plasma, either by direct advection from neutral winds or electrodynamic coupling to the neutral wave signatures.

This study showcases the potential of combining a high-resolution regional wave model for source modeling with a global IT general circulation model to study the subsequent variability in the ionosphere perturbed by terrestrial weather from below. The waves, nudged at the lower levels (E-region and lower F-region) of the IT model, cover a broad wave spectrum, with the dominant wave signals matching the F region ionospheric observations. Given the capability of the IT model to also simulate the influences of space storms realistically on the IT from above (Lu et al., 2023), this setup can be used to explore the relative contribution, interplay, and preconditioning effects of these two important sources in determining the variability of the geospace system.

Acknowledgement

X. Lu and H. Wu's work is supported by NASA grants 80NSSC22K0018, NNX17AG10G, 80NSSC22K1010, 80NSSCK19K0810, and NSF grants AGS-2012994, CAREER-1753214. The team acknowledges the NSF/ANSWERS grants AGS-2149695, AGS-2149696, AGS-2149697, and AGS-2149698, which foster this collaborative work. GNSS TEC data processing and Madrigal database system are provided to the community by MIT under NSF grant AGS-1952737 support. S. Zhang's work was supported by NASA grants 80GSFC22CA011, 80NSSC21K1310, and 80NSSC22K1074.

Open Research

The data from the TIEGCN-NG simulation and the codes used to read and plot the figures are available at https://data.mendeley.com/datasets/689dzcy8wv. The ICON data were obtained from https://icon.ssl.berkeley.edu/Data/Data-Product-Matrix. The COSMIC-II data were obtained from http://formosat7.earth.ncku.edu.tw/. The National Center for Atmospheric Research is sponsored by the National Science Foundation.

Reference

Azeem, I., J. Yue, L. Hoffmann, S. D. Miller, W. C. Straka III, and G. Crowley (2015), Multisensor profiling of a concentric gravity wave event propagating from the troposphere to the ionosphere, Geophys. Res. Lett., 42, 7874–7880, doi:10.1002/ 2015GL065903.

Bale, D. S., LeVeque, R. J., Mitran, S., & Rossmanith, J. A. (2002). A wave propagation method for conservation laws and balance laws with spatially varying flux functions. Journal of Scientific Computing, 24(3), 955–978.

Becker, E., Vadas, S. L., Bossert, K., Harvey, V. L., Zülicke, C., & Hoffmann, L. (2022). A High-resolution whole- atmosphere model with resolved gravity waves and specified large-scale dynamics in the troposphere and stratosphere. Journal of Geophysical Research: Atmospheres, 127, e2021JD035018. https://doi.org/10.1029/2021JD035018

Bishop, R. L., Aponte, N., Earle, G. D., Sulzer, M., Larsen, M. F., and Peng, G. S. (2006), Arecibo observations of ionospheric perturbations associated with the passage of Tropical Storm Odette, J. Geophys. Res., 111, A11320, doi:10.1029/2006JA011668.

Bossert, K., Paxton, L. J., Matsuo, T., Goncharenko, L., Kumari, K., & Conde, M. (2022). Large-scale traveling atmospheric and ionospheric disturbances observed in GUVI with multi-instrument validations. Geophysical Research Letters, 49, e2022GL099901. https://doi. org/10.1029/2022GL099901

Chen, C., X. Chu, A. J. McDonald, S. L. Vadas, Z. Yu, W. Fong, and X. Lu (2013), Inertia-gravity waves in Antarctica: A case study with simultaneous lidar and radar measurements at McMurdo/Scott Base(77.8S, 166.7E), J. Geophys. Res. Atmos., 118, doi:10.1002/jgrd.50318.

Chen, C., X. Chu, J. Zhao, B. R. Roberts, Z. Yu, W. Fong, X. Lu, J. A. Smith (2016), Lidar observations of persistent inertia-gravity waves with periods of 3–10 h in the Antarctic middle and upper atmosphere at McMurdo, J. Geophys. Res. Space Physics., 121, doi:10.1002/2015JA022127.

Chou, M. Y., Lin, C. C. H., Yue, J., Tsai, H. F., Sun, Y. Y., Liu, J. Y., and Chen, C. H. (2017), Concentric traveling ionosphere disturbances triggered by Super Typhoon Meranti (2016), Geophys. Res. Lett., 44, 1219–1226, doi:10.1002/2016GL072205

Chou M-Y, Braun JJ, Wu Q, Heelis RA, Zakharenkova I, Cherniak I, Pedatella NM, Stoneback RA. (2021). Validation of FORMOSAT-7/COSMIC2 IVM ion density and TGRS orbit electron density. Terr Atmos Ocean Sci 32:939–951. https://doi.org/10.3319/TAO.2021.06.22.01

Cullens, C. Y., Thurairajah, B., England, S. L., Randall, C. E., Yue, J., & Wright, C. (2023). Observations of typhoon generated gravity waves from the CIPS and AIRS instruments and comparison to the high-resolution ECMWF model. Journal of Geophysical Research: Atmospheres, 128, e2022JD038170. https://doi.org/10.1029/2022JD038170

England, S. L., Greer, K. R., Zhang, S.-R., Evans, S., Solomon, S. C., Eastes, R. W., et al. (2021). First comparison of traveling atmospheric disturbances observed in the middle thermosphere by Global-scale Observations of the Limb and Disk to traveling ionospheric disturbances seen in ground-based total electron content observations. Journal of Geophysical Research: Space Physics, 126, e2021JA029248. https://doi. org/10.1029/2021JA029248

Feggeler, M., and England, S.L., (2024), Ionospheric observations from formation flying spacecraft, Advances in Space Research, 0273-1177, https://doi.org/10.1016/j.asr.2024.03.054. Fritts, D., and Alexander, M., (2003), Gravity wave dynamics and effects in the middle atmosphere, Rev. Geophys., 41(1), 1003, doi:10.1029/2001RG000106.

Gong, J., Yue, J., and Wu, D. L. (2015), Global survey of concentric gravity waves in AIRS images and ECMWF analysis, J. Geophys. Res. Atmos., 120, 2210–2228, doi:10.1002/2014JD022527.

Harvey, V. L., Randall, C. E., Goncharenko, L. P., Becker, E., Forbes, J. M., Carstens, J., et al. (2023). CIPS observations of gravity wave activity at the edge of the polar vortices and coupling to the ionosphere. Journal of Geophysical Research: Atmospheres, 128, e2023JD038827. https://doi.org/10.1029/2023JD038827

Heale, C. J., Snively, J. B., Bhatt, A. N., Hoffmann, L., Stephan, C. C., & Kendall, E. A. (2019). Multilayer observations and modeling of thunderstorm-generated gravity waves over the Midwestern United States. Geophysical Research Letters, 46, 14,164–14,174. https://doi.org/10. 1029/2019GL085934

Heale, C. J., and J. B. Snively (2015), Gravity wave propagation through a vertically and horizontally inhomogeneous background wind, J. Geophys. Res. Atmos., 120, doi:10.1002/2015JD023505.

Heelis, R.A, R.A. Stoneback, M.D. Perdue, M.P. Depew, Z.A. Morgan, M.D. Mankey, C.R. Lippincott, L.L. Harmon, B.J. Holt (2017), Ion velocity measurements for the Ionospheric Connections Explorer. Space Sci. Rev., doi:10.1007/s11214-017-0383-3

Heelis, R.A., Depew, M.D., Chen, Y.J. and Perdue, M.D., (2022). Ionospheric Connections (ICON) Ion Velocity Meter (IVM) Observations of the Equatorial Ionosphere at Solar Minimum. Space Science Reviews, 218(8), pp.1-16. DOI: 10.1007/s11214-022-00936-w

Huba, J. D., D. P. Drob, T.-W. Wu, and J. J. Makela (2015), Modeling the ionospheric impact of tsunami-driven gravity waves with SAMI3: Conjugate effects, Geophys. Res. Lett., 42, 5719–5726, doi:10.1002/2015GL064871.

Huba, J. D., Becker, E., & Vadas, S. L. (2023a). Simulation study of the 15 January 2022 Tonga event: Development of super equatorial plasma bubbles. Geophysical Research Letters, 50, e2022GL101185. https://doi. org/10.1029/2022GL101185

Huba, J. D., Liu, H.-L., & McInerney, J. (2023b). Modeling the development of an equatorial plasma bubble during a midnight temperature maximum with SAMI3/WACCM-X. Geophysical Research Letters, 50, e2023GL104388. https://doi.org/10.1029/2023GL104388

Leonard, J. M., J. M. Forbes, and G. H. Born (2012), Impact of tidal density variability on orbital and reentry predictions, Space Weather, 10, S12003, doi:10.1029/2012SW000842.

LeVeque, R. J. (2002). Finite volume methods for hyperbolic problems. Cambridge University Press (ISBN: ISBN-0-521-00924-3).

Liu, H.-L., J. M. McInerney, S. Santos, P. H. Lauritzen, M. A. Taylor, and N. M. Pedatella (2014), Gravity waves simulated by high-resolution Whole Atmosphere Community Climate Model, Geophys. Res. Lett., 41, doi:10.1002/2014GL062468.

Liu, H.-L., Wang, W., Huba, J. D., Lauritzen, P. H., & Vitt, F. (2023). Atmospheric and ionospheric responses to Hunga-Tonga volcano eruption simulated by WACCM-X. Geophysical Research Letters, 50, e2023GL103682. https://doi. org/10.1029/2023GL103682

Liu, H.-L., Lauritzen, P. H., & Vitt, F. (2024). Impacts of gravity waves on the thermospheric circulation and composition. Geophysical Research Letters, 51, e2023GL107453. https://doi. org/10.1029/2023GL107453

Lu, X., A. Z. Liu, G. R. Swenson, T. Li, T. Leblanc, and I. S. McDermid (2009), Gravity wave propagation and dissipation from the stratosphere to the lower thermosphere, J. Geophys. Res., 114, D11101, doi:10.1029/2008JD010112.

Lu, X., C. Chen, W. Huang, J. A. Smith, X. Chu, T. Yuan, P.-D. Pautet, M. J. Taylor, J. Gong, and C. Y. Cullens (2015a), A coordinated study of 1 h mesoscale gravity waves propagating from Logan to Boulder with CRRL Na Doppler lidars and temperature mapper, J. Geophys. Res. Atmos., 120, doi:10.1002/2015JD023604.

Lu, X., X. Chu, W. Fong, C. Chen, Z. Yu, B. R. Roberts, and A. J. McDonald (2015b), Vertical evolution of potential energy density and vertical wave number spectrum of Antarctic gravity waves from 35 to 105 km at McMurdo (77.8°S, 166.7°E), J. Geophys. Res. Atmos., 120, 2719–2737. doi: 10.1002/2014JD022751.

Lu, X., X. Chu, H. Li, C. Chen, J. Smith, S. Vadas (2017), Statistical characterization of high-to-medium frequency mesoscale gravity waves by lidar-measured vertical winds and temperatures in the MLT, J. Atmos. Solar- Terr. Phys.,162, 3-15 doi:10.1016/j.jastp.2016.10.009.

Lu, X., Wu, H., Kaeppler, S., Meriwether, J., Nishimura, Y., Wang, W., et al. (2023). Understanding strong neutral vertical winds and ionospheric responses to the 2015 St. Patrick's Day storm using TIEGCM driven by data-assimilated aurora and electric fields. Space Weather, 21, e2022SW003308. https://doi. org/10.1029/2022SW003308

Nicolls, M. J., and Kelley, M. C. (2005). Strong evidence for gravity wave seeding of an ionospheric plasma instability, Geophys. Res. Lett.,32, L05108, doi:10.1029/2004GL020737.

Qian, L., Burns, A. G., Emery, B. A., Foster, B., Lu, G., Maute, A., Richmond, A. D., Roble, R. G., Solomon, S. C., and Wang, W. (2014), The NCAR TIE-GCM: A Community Model of the Coupled Thermosphere/Ionosphere System, Geophysical Monograph Series, American Geophysical Union, doi:10.1002/9781118704417.ch7

Richmond, A. D., Ridley, E. C., and Roble, R. G. (1992), A thermosphere/ionosphere general circulation model with coupled electrodynamics, Geophysical Research Letters, 19(6), 601-604, doi:10.1029/92GL00401

Rideout, W. & Coster, A. (2006). Automated GPS processing for global total electron content data. *GPS Solutions*, *10*(3), 219–228. https://doi.org/10.1007/s10291-006-0029-5

Savitzky, A. & Golay, M. J. E. (1964). Smoothing and Differentiation of Data by Simplified Least Squares Procedures. *Analytical Chemistry*, *36*(8), 1627–1639. https://doi.org/10.1021/ac60214a047

Shinbori, A., Otsuka, Y., Sori, T., Nishioka, M., Perwitasari, S., Tsuda, T., & Nishitani, N. (2022). Electromagnetic conjugacy of ionospheric disturbances after the 2022 Hunga Tonga-Hunga Ha'apai volcanic eruption as seen in GNSS-TEC and SuperDARN Hokkaido pair of radars observations. Earth Planets and Space, 74(1), 106. https://doi.org/10.1186/s40623-022-01665-8

Snively, J. B. (2013). Mesospheric hydroxyl airglow signatures of acoustic and gravity waves generated by transient tropospheric forcing. Geophysical Research Letters, 40, 4533–4537. https://doi.org/10.1002/grl.50886

Snively, J. B., & Pasko, V. P. (2008). Excitation of ducted gravity waves in the lower thermosphere by tropospheric sources. Journal of Geophysical Research, 113, A06303. https://doi.org/10.1029/2007JA012693

Stephan, C. C., & Alexander, M. J. (2015). Realistic simulations of atmospheric gravity waves over the continental U.S. using precipitation radar data. Journal of Advances in Modeling Earth Systems, 7, 823–835. https://doi.org/10.1002/2014MS000396

Takahashi, H., Wrasse, C. M., Figueiredo, C. A. O. B., Barros, D., Paulino, I., Essien, P., et al. (2020). Equatorial plasma bubble occurrence under propagation of MSTID and MLT gravity waves. Journal of Geophysical Research: Space Physics,125,e2019JA027566. https://doi.org/10.1029/2019JA027566

Vadas, S. L., Figueiredo, C., Becker, E., Huba, J. D., Themens, D. R., Hindley, N. P., et al. (2023). Traveling ionospheric disturbances induced by the secondary gravity waves from the Tonga eruption on 15 January 2022: Modeling with MESORAC-HIAMCM-SAMI3 and comparison with GPS/TEC and ionosonde data. Journal of Geophysical Research: Space Physics, 128, e2023JA031408. https://doi.org/10.1029/2023JA031408

Vadas, S.L., Fritts, D.C. (2005). Thermospheric responses to gravity waves: influences of increasing viscosity and thermal diffusivity. J. Geophys. Res. 110, D15103. http:// dx.doi.org/10.1029/2004JD005574.

Vadas, S.L. (2013). Compressible f-plane solutions to body forces, heatings, and coolings, and application to the primary and secondary gravity waves generated by a deep convective plume. J. Geophys. Res. Space Phys. 118, 2377–2397. http://dx.doi.org/10.1002/jgra.50163.

Vadas, S., J. Yue, and T. Nakamura (2012), Mesospheric concentric gravity waves generated by multiple convectivestorms over the North American Great Plain,J. Geophys. Res.,117, D07113, doi:10.1029/2011JD017025

Varney, R. H., Kelley, M. C. , and Kudeki, E. (2009), Observations of electric fields associated with internal gravity waves, J. Geophys. Res., 114, A02304, doi:10.1029/2008JA013733.

Vierinen, J., Coster, A. J., Rideout, W. C., Erickson, P. J. & Norberg, J. (2016). Statistical framework for estimating GNSS bias. Atmos. Meas. Tech., 9, 1303–1312, https://doi.org/10.5194/amt-9-1303-2016.

Wu, H., and Lu, X. (2022), Data assimilation of high-latitude electric fields: Extension of a multi-resolution Gaussian process model (Lattice Kriging) to vector fields, Space Weather, 20(1), e2021SW002880, doi:10.1029/2021SW002880

Wu, H., Tan, X., Zhang, Q., Huang, W., Lu, X., Nishimura, Y., & Zhang, Y. (2022). Multiresolution data assimilation for auroral energy flux and mean energy using DMSP SSUSI, THEMIS ASI, and an empirical model. Space Weather, 20, e2022SW003146. https://doi. org/10.1029/2022SW003146.

Wu, H., Lu, X., Wang, W., & Liu, H.-L. (2023). Simulation of the propagation and effects of gravity waves generated by Tonga volcano eruption in the thermosphere and ionosphere using nested-grid TIEGCM. Journal of Geophysical Research: Space Physics, 128, e2023JA031354. https://doi. org/10.1029/2023JA031354

Yue, J., B. Thurairajah, L. Hoffmann, J. Alexander, A. Chandran, M. J. Taylor, J. M. Russell III, C. E. Randall, and S. M. Bailey (2014), Concentric gravity waves in polar mesospheric clouds from the Cloud Imaging and Particle Size experiment, J. Geophys. Res. Atmos., 119, 5115–5127, doi:10.1002/ 2013JD021385.

Zhao, Y., Deng, Y., Wang, J.-S., Zhang, S.-R., Lin, C. Y. (2020). Tropical cyclone-induced gravity wave perturbations in the upper atmosphere: GITM-R simulations. Journal of Geophysical Research: Space Physics, 125, e2019JA027675. https://doi.org/ 10.1029/2019JA027675

Zhang, S.-R., Erickson, P. J., Goncharenko, L. P., Coster, A. J., Rideout, W. & Vierinen, J. (2017). Ionospheric Bow Waves and Perturbations Induced by the 21 August 2017 Solar Eclipse. *Geophysical Research Letters*, *44*(24), 12,067-12,073. https://doi.org/10.1002/2017gl076054

Zhang, S., Erickson, P. J., Gasque, L. C., Aa, E., Rideout, W., Vierinen, J., Goncharenko, L. P. & Coster, A. J. (2021). Electrified Postsunrise Ionospheric Perturbations at Millstone Hill. *Geophysical Research Letters*, *48*(18), e2021GL095151. https://doi.org/10.1029/2021gl095151

Zhang, S.-R., Nishimura, Y., Erickson, P. J., Aa, E., Kil, H., Deng, Y., Thomas, E. G., Rideout, W., Coster, A. J., Kerr, R. & Vierinen, J. (2022). Traveling Ionospheric Disturbances in the Vicinity of Storm-Enhanced Density at Midlatitudes. *Journal of Geophysical Research: Space Physics*, *127*(8), e2022JA030429. https://doi.org/10.1029/2022ja030429

Zhang, S.-R., Nishimura, Y., Vierinen, J., Lyons, L. R., Knipp, D. J., Gustavsson, B. J., Waghule, B. V., Erickson, P. J., Coster, A. J., Aa, E. & Spicher, A. (2023). Simultaneous Global Ionospheric Disturbances Associated With Penetration Electric Fields During Intense and Minor Solar and Geomagnetic Disturbances. *Geophysical Research Letters*, *50*(19), e2023GL104250. https://doi.org/10.1029/2023gl104250

Figure 1. (a) NOAA Tornado reports in April 2020. (b) NEXRAD Reflectivity at 21:55 UTC. (c) AIRS composite 4.3- and 8.1-micron observations at 18:00 UTC on 12 April 2020.

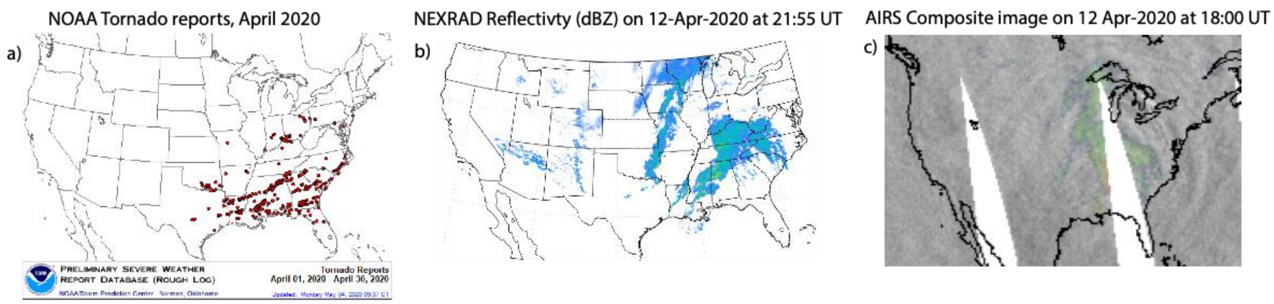

Figure 2. MAGIC simulated temperatures at z=50 km, 100km, and 250 km at 21:55 UTC with the NEXRAD reflectivity maps overlaid.

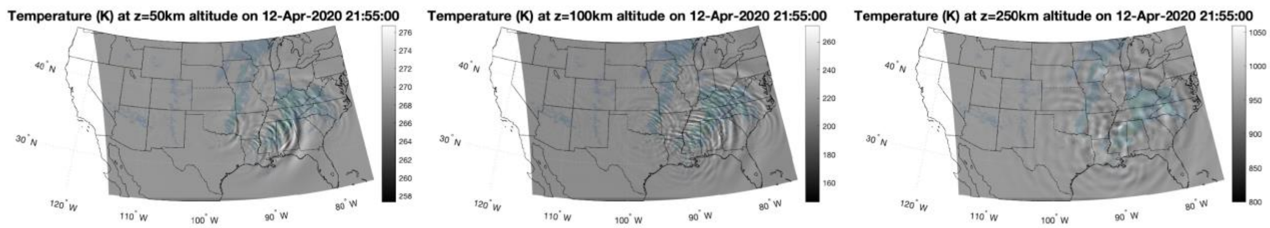

Figure 3. (a1-a3) GNSS dTEC observations at the initial (21:50 UTC), evolving (23:45 UTC), and peak (25:15 UTC) phases, respectively. (b1-b3) are similar except for the TIEGCM-NG simulations. Three black dashed lines in (a3) and (b3) are the three slices for the wavelet analysis in Figure 4.

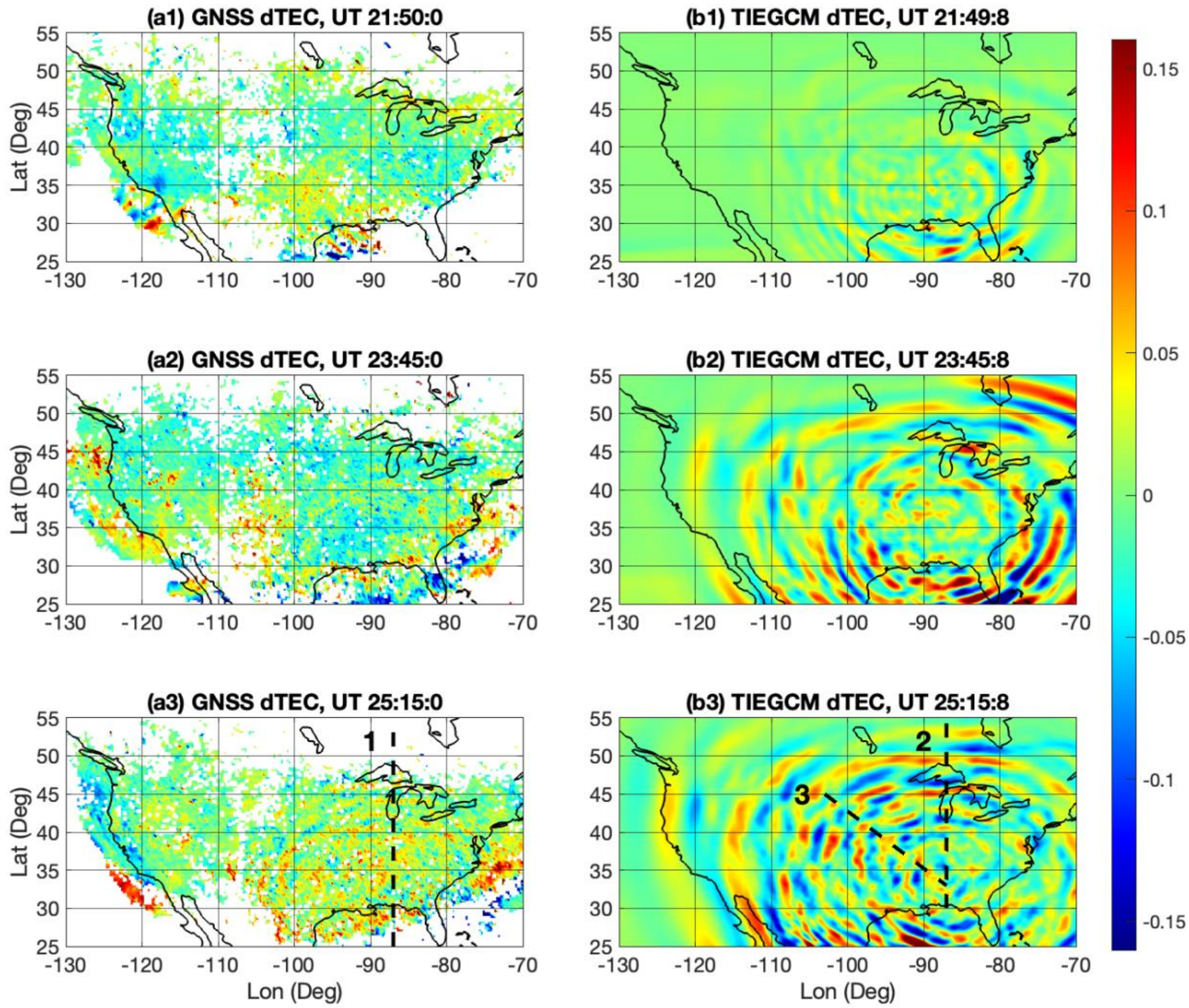

Figure 4. (a1–c1) dTECs along the trajectories 1, 2, and 3 (dashed black lines in Figures 3a3 and 3b3). (a2–c2) their corresponding wavelet spectra in amplitudes.

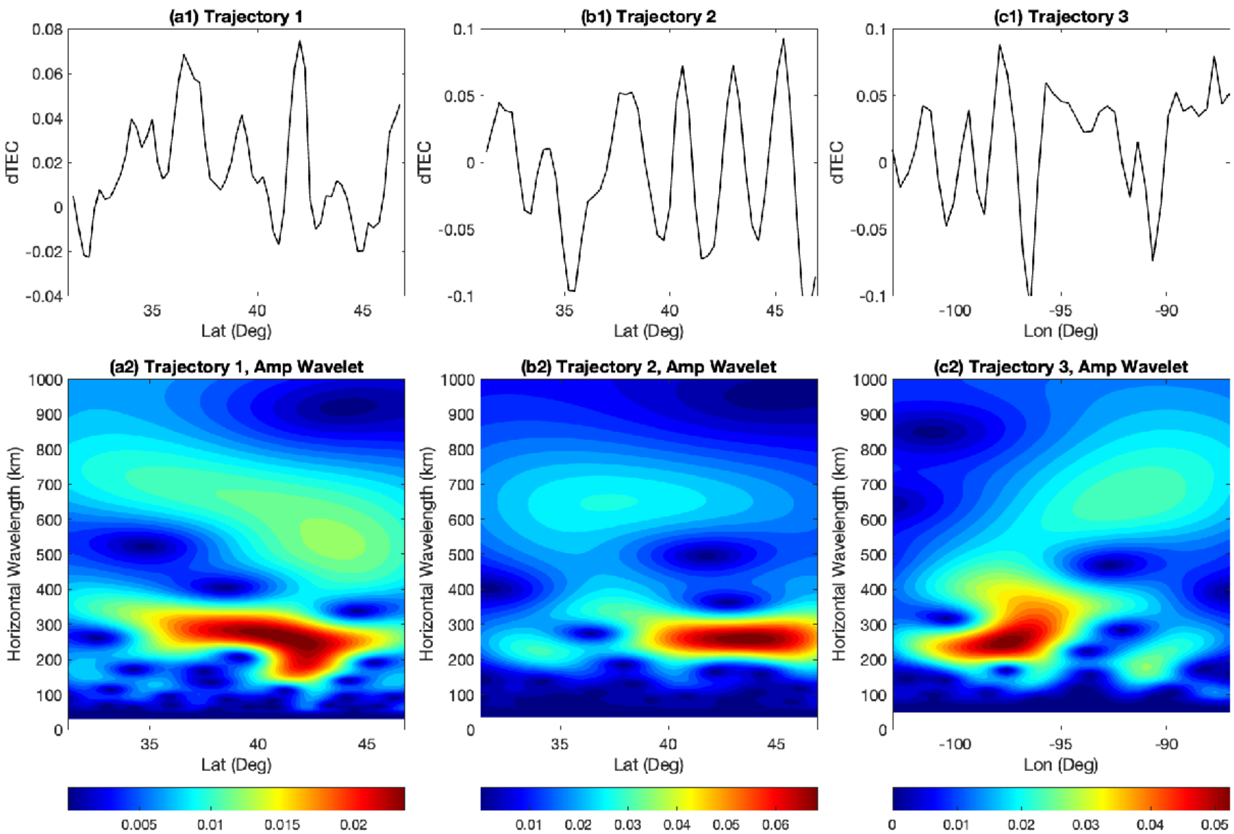

Figure 5. (a1-a3) Keograms of dTECs from GNSS observations along longitudes of -95°, -88°, and -81°, respectively. (b1-b3) are the same except for dTECs obtained from TIEGCM-NG. (c1-c3) are the same as (b1-b3) except for relative dTECs (unit of %) derived as dTEC/background TEC. Dashed lines in the middle column highlight wave fronts used for the calculation of horizontal phase speeds.

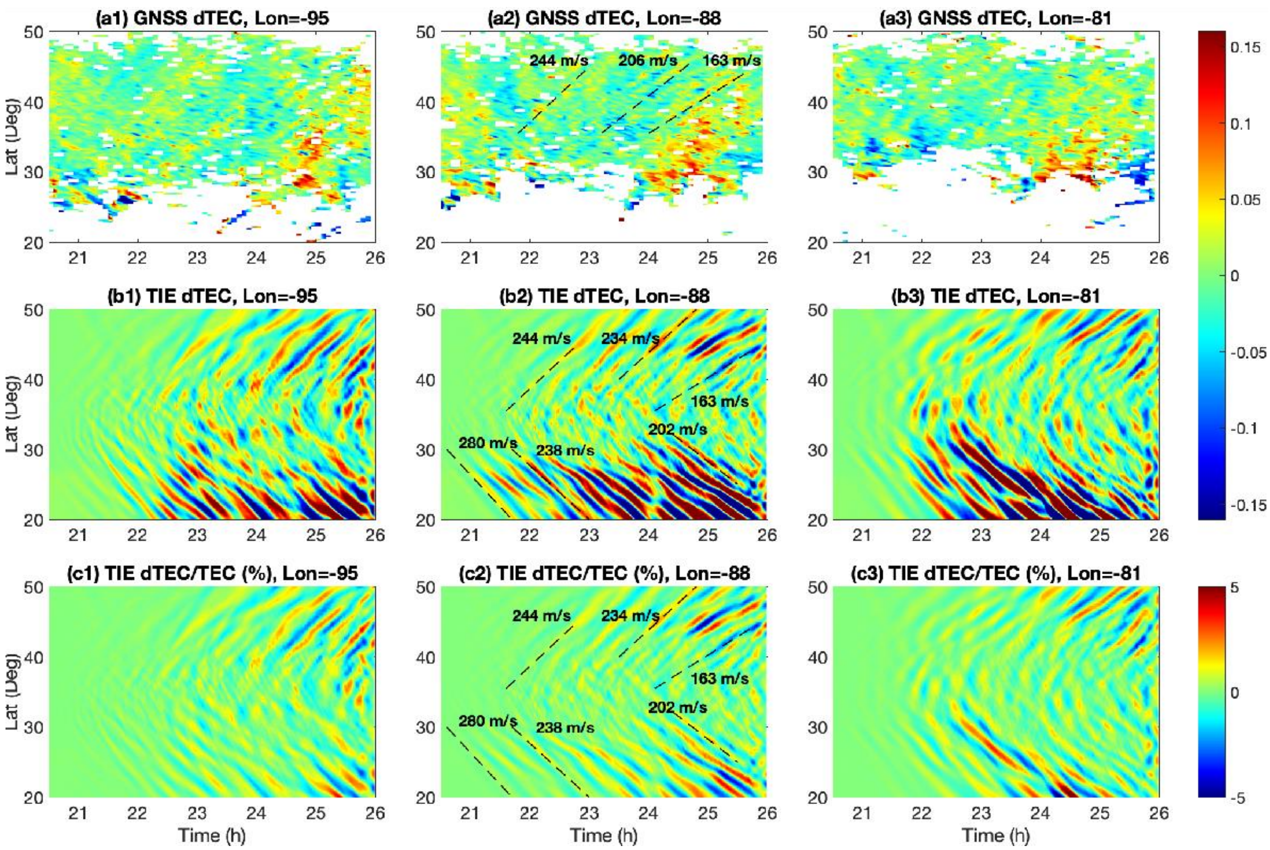

Figure 6. (a1-d1) Differential wave fields in zonal, meridional, vertical winds, and temperature at 200 km. (a2-d2) are the same except for 400 km. Unit is m/s for wind and K for temperature.

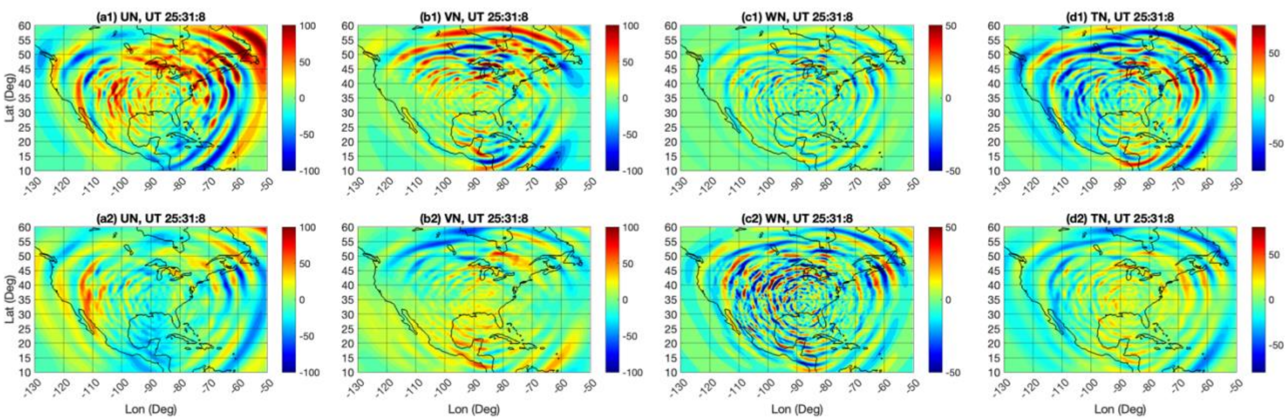

Figure 7. Wave-induced perturbations in (a) zonal wind, (b) meridional wind, (c) vertical wind, and (d) temperature at the location of lon=-85°, lat=40°. (e) and (f) show the horizontal slices of these perturbations with time at 200 and 400 km, respectively.

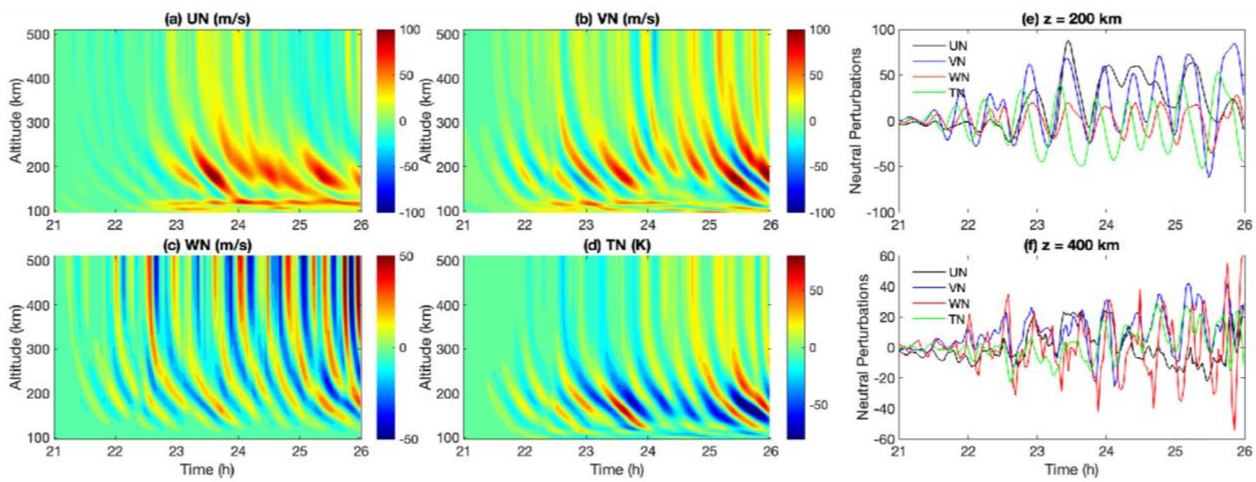

Figure 8. (a1-d1) Wavelet amplitude spectra for neutral winds (unit: m/s) and temperature (unit: K) based on the wave perturbations in Figure 7e at 200 km. (a2-d2) are the same except for Figure 7f at 400 km.

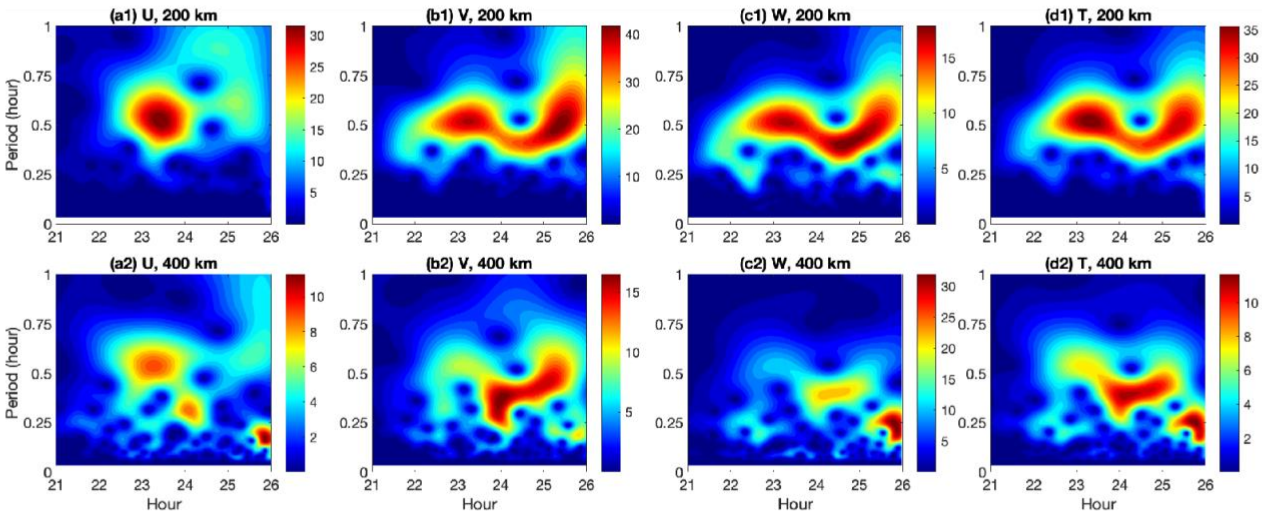

Figure 9. (a1-c1) Absolute electron density distributions at the same timings, corresponding to the initial, evolving, and peak phases, as Figure 3 at 200 km. (a2-c2) and (a3-c3) are the same except for 250 and 400 km, respectively. Unit is $10^5/cm^3$.

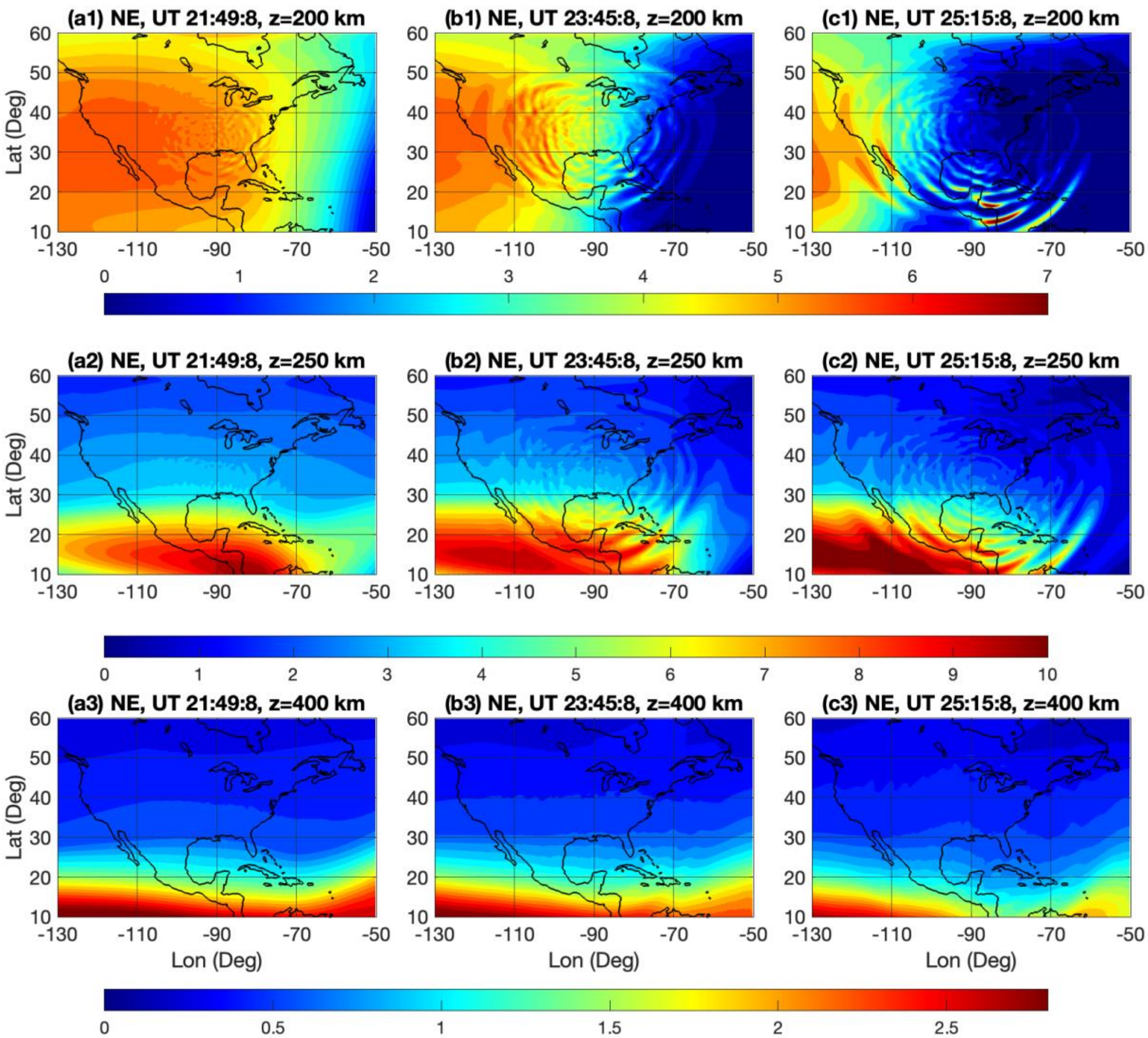

Figure 10. Same as Figure 9 except for the relative perturbations in neutral density. Note that the color bars are different for the three rows.

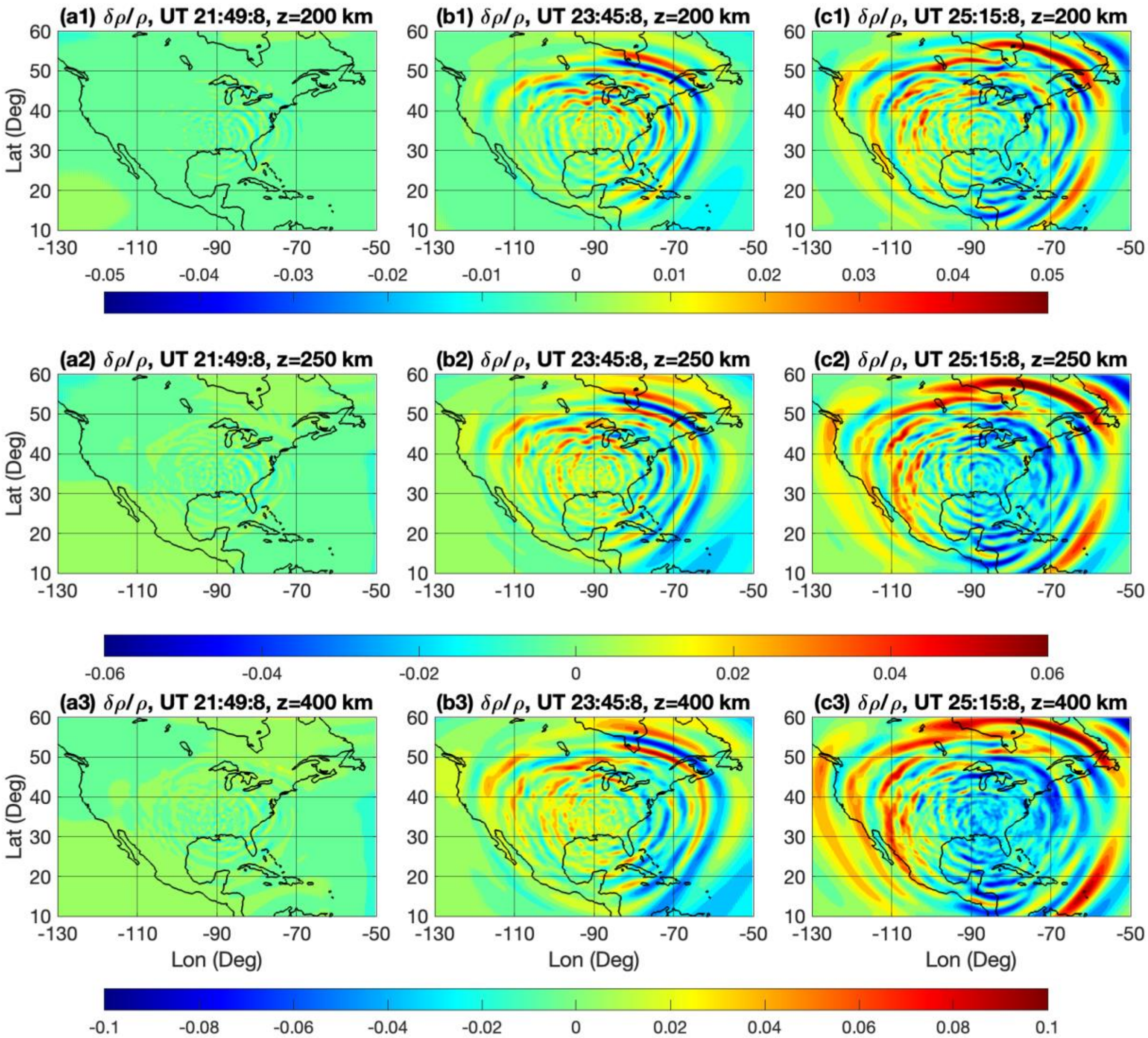

Figure 11. (a1-c1) Perturbations in zonal, meridional, and vertical ion drifts (UI, VI, and WI) at 23:05 UTC. (a2-c2) are the same except for 24:55 UTC. Unit is m/s.

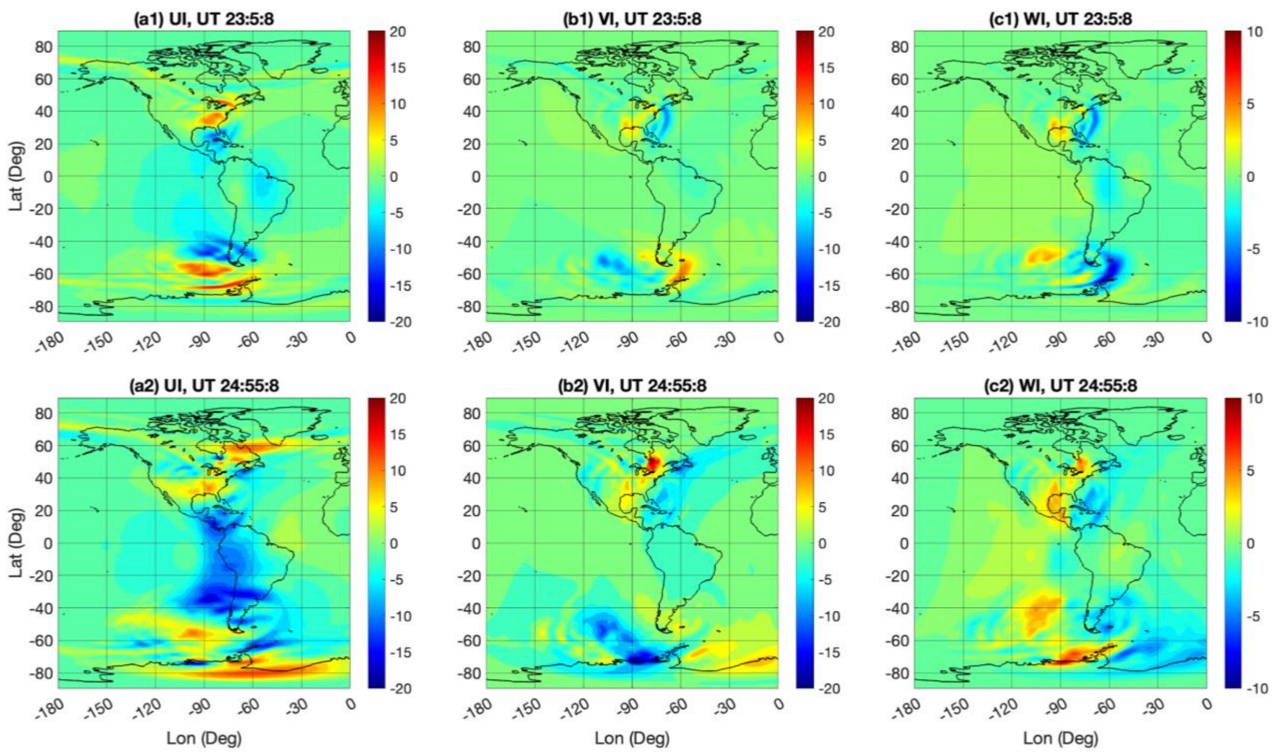

Figure 12. In situ ion observations from ICON and their comparison to the TIEGCM-NG results. (a) 3 segments of orbits during which ICON is in the vicinity of the event. The color coding of each of the 3 segments is reflected in the remaining panels. The purple dashed line marks the boundary of the high resolution nested grid (b–d) Detrended in situ ion densities observed with ICON and simulated with TIEGCM-NG at the closest available point (see text). Each corresponds to the measurements along the curved orbit tracks shown, and as a function of longitude. (e–g) Lomb-Scargle periodograms of the detrended ion densities from ICON (color) and the TIEGCM-NG model (black). The scale for each is as seen along the curved orbit, shown in degrees longitude. (h–j) Detrended O^+ fraction (relative to the total number of ions) observed.

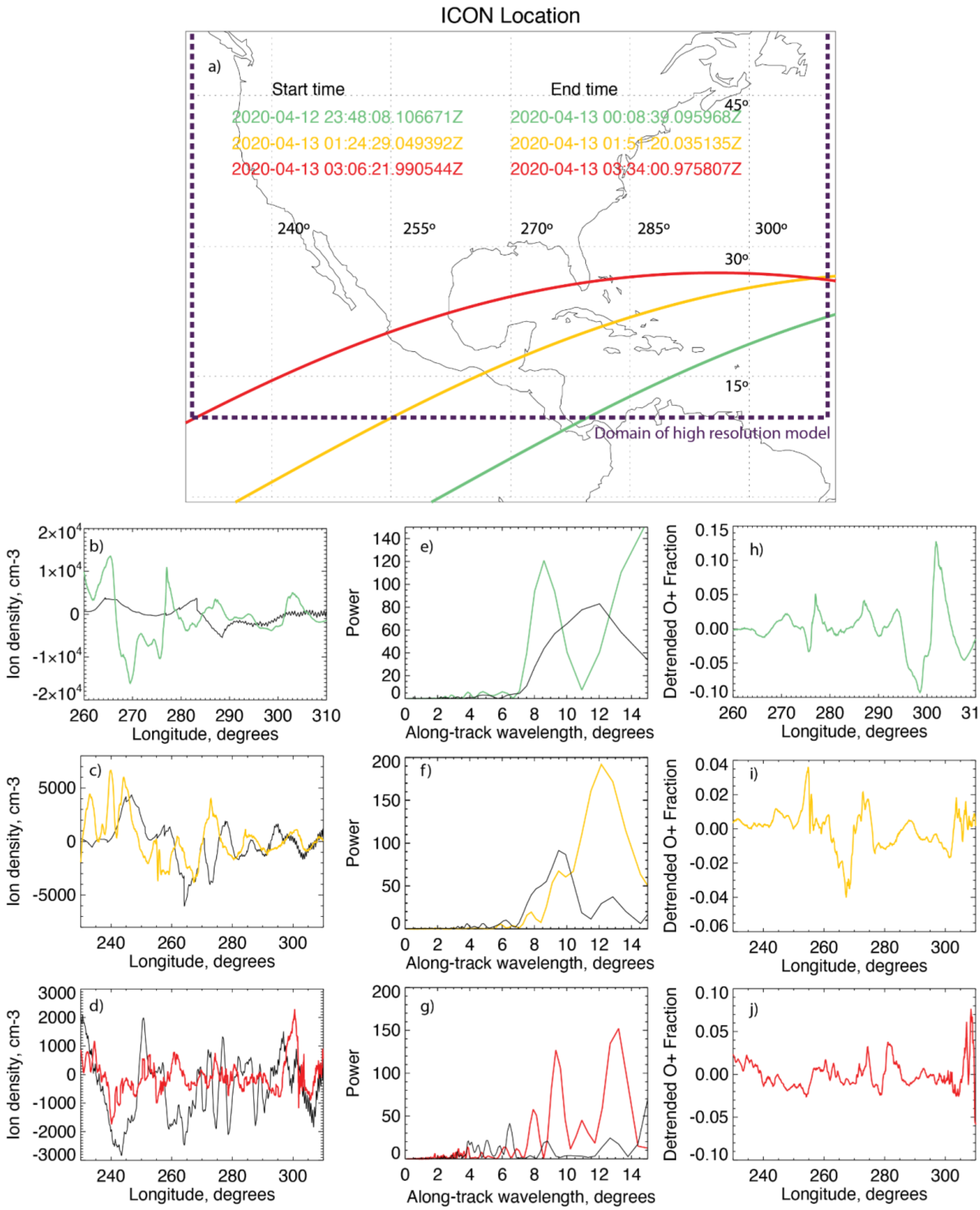
ICON Location
a)
Start time
End time
2020-04-12 23:48:08.106671Z
2020-04-13 00:08:39.095968Z
2020-04-13 01:24:29.049392Z
2020-04-13 01:51:20.035135Z
2020-04-13 03:06:21.990544Z
2020-04-13 03:34:00.975807Z
45°
30°
15°
240°
255°
270°
285°
300°
Domain of high resolution model
b)
c)
d)
e)
f)
g)
h)
i)
j)
Ion density, cm-3
Longitude, degrees
Power
Along-track wavelength, degrees
Detrended O+ Fraction

Figure 13. Same as Figure 12, but for COSMIC-2 FM1 and FM4. Panels b-f shows the detrended in situ ion densities and panels g -k show the corresponding periodograms.

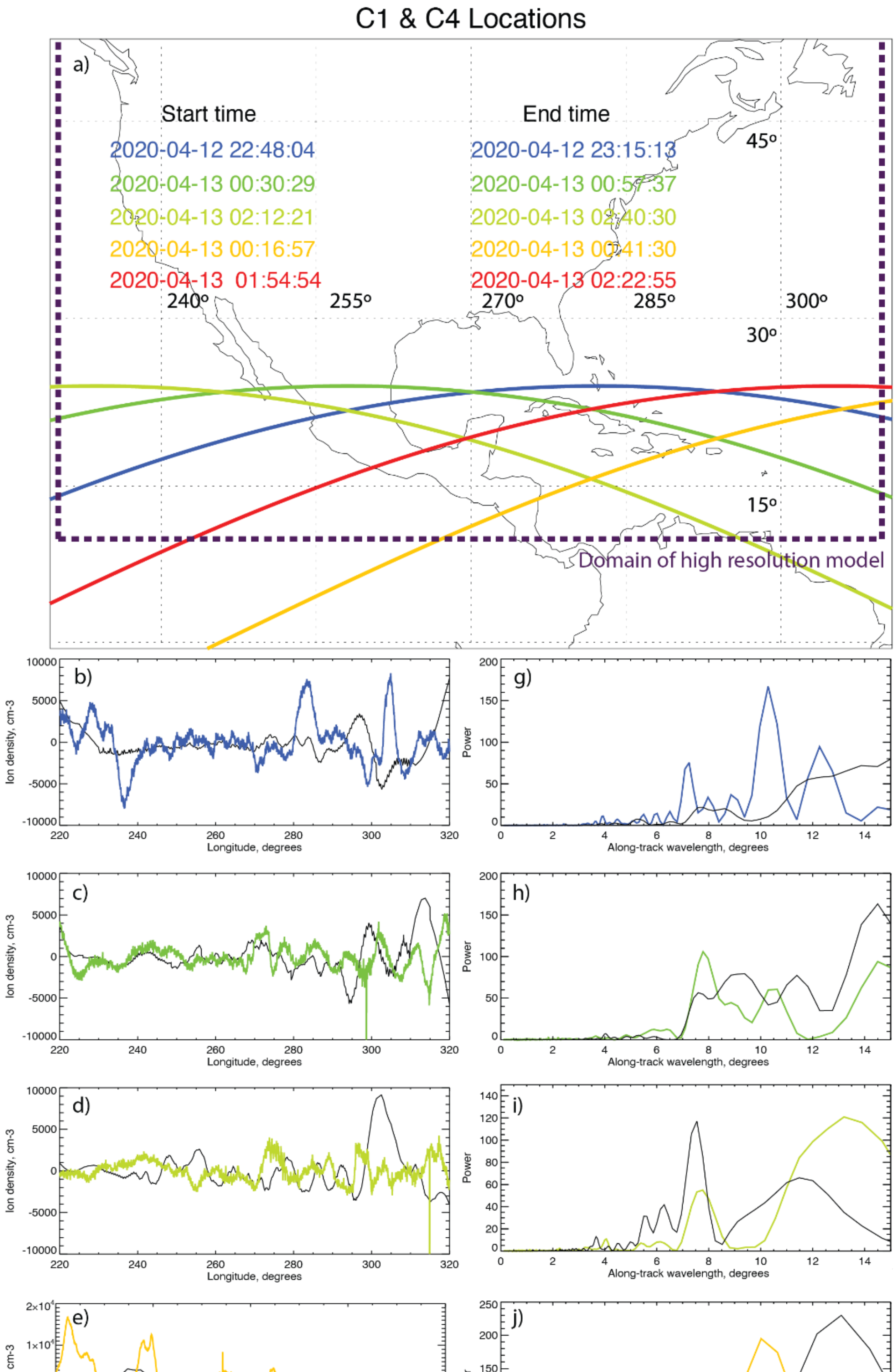
C1 & C4 Locations
a)
Start time
End time
2020-04-12 22:48:04
2020-04-13 00:30:29
2020-04-13 02:12:21
2020-04-13 00:16:57
2020-04-13 01:54:54
2020-04-12 23:15:13
2020-04-13 00:57:37
2020-04-13 02:40:30
2020-04-13 00:41:30
2020-04-13 02:22:55
45°
30°
15°
240°
255°
270°
285°
300°
Domain of high resolution model
b)
c)
d)
e)
g)
h)
i)
j)
Ion density, cm-3
Longitude, degrees
Power
Along-track wavelength, degrees